GEOPHYSICS, VOL. 76, NO. 3 (MAY-JUNE 2011); P. WA71–WA82, 11 FIGS.
10.1190/1.3560018

V_P/V_S ratio and shear-wave splitting in the Nankai Trough seismogenic zone: Insights into effective stress, pore pressure, and sediment consolidation

Takeshi Tsuji[1], Jack Dvorkin[2], Gary Mavko[2], Norimitsu Nakata[1], Toshifumi Matsuoka[1], Ayako Nakanishi[3], Shuichi Kodaira[3], and Osamu Nishizawa[4]

ABSTRACT

To estimate variation of stress state and sediment consolidation in the Nankai plate subduction zone off southwest Japan, we measured the P-wave to S-wave velocity ratio (V_P/V_S) and S-wave splitting along the seismic line extending from the trench to the seismogenic zone. For this purpose, we used active-source seismic data recorded by multicomponent ocean bottom seismometers (OBS). Because it is difficult to identify the PS-converted reflection waveforms for each of the geological boundaries in this deep offshore region, we focused on the more easily identified PPS-refracted waveforms that register the conversion of the up-going P-waves to S-waves at the igneous crust surface. We estimated the average V_P/V_S ratio within the sedimentary section by using the time lag between the P-refracted waves and PPS-converted waves. This V_P/V_S ratio changes abruptly at the trough axis (i.e., the deformation front of the accretionary prism) arguably because of compaction associated with the accretion process. We observed relatively high V_P/V_S around the seismogenic megasplay fault, which may partially indicate the abnormal pore pressure and intensive fractures associated with the fault. To estimate the stress-induced fracture orientation and stress magnitude, we computed the fast S-wave polarization direction and estimated S-wave velocity anisotropy by applying the crosscorrelation method to the PPS-converted waves. To improve signal-to-noise ratio of the waveform for S-wave splitting analysis, we stacked PPS-converted waveforms on receiver gather. These anisotropic characteristics change at the seismogenic megasplay fault: the fast polarization direction is nearly parallel to the subduction direction seaward of the megasplay fault and is perpendicular to the subduction direction landward of the megasplay fault. This velocity anisotropy is especially strong around the megasplay fault. These results imply that the preferred fracture orientation, as well as the principal stress orientation, is oblique to the direction of plate subduction near the megasplay fault.

INTRODUCTION

The Nankai Trough is a convergent plate margin where the Philippine Sea plate is subducting beneath southwest Japan (Figure 1). This subduction zone has repeatedly generated great earthquakes in excess of M8 (Ando, 1975). Because large earthquakes at the convergent plate margins have been assumed to occur along the subduction interface, as well as megasplay faults, many seismic surveys have been conducted to characterize the seismogenic fault (e.g. Moore et al., 1990; Park et al., 2002; Bangs et al., 2004; Tsuji et al., 2005; Kodaira et al., 2006; Nakanishi et al., 2008; Moore et al., 2009). Because high pore pressure near a fault acts to reduce the effective stress (which presumably lowers the fault's strength), the development of abnormal pore pressures influences the shallow limit of seismogenic faulting (e.g., Scholz, 1998; Moore and Saffer, 2001). Therefore, the pore pressure within an accretionary prism is a key parameter in evaluating seismogenic fault activity. Several seismic studies have used the P-wave velocity (V_P) to estimate the pore pressure and effective stress around seismogenic faults

Manuscript received by the Editor 22 September 2010; revised manuscript received 27 December 2010; published online 23 May 2011.
[1]Kyoto University, Graduate School of Engineering, Kyoto, Japan. E-mail: tsuji@earth.kumst.kyoto-u.ac.jp; n_nakata@earth.kumst.kyoto-u.ac.jp; matsuoka@earth.kumst.kyoto-u.ac.jp.
[2]Stanford University, Department of Geophysics, Stanford Rock Physics Laboratory, Stanford, California, U.S.A. E-mail: dvorkin@stanford.edu; mavko@stanford.edu.
[3]Japan Agency for Marine-Earth Science and Technology (JAMSTEC), Kanagawa, Japan. E-mail: ann@jamstec.go.jp; kodaira@jamstec.go.jp.
[4]Research Institute of Innovative Technology for the Earth (RITE), Kyoto, Japan. E-mail: epchan85 @rite.or.jp.

(e.g., Tsuji et al., 2008; Tobin and Saffer, 2009). However, information from V_P alone is insufficient to predict the pore pressure distribution within an accretionary prism because the accretion process causes spatial changes in the sediment's compaction/consolidation and the effective stress orientation.

The S-wave velocity (V_S) is an important parameter in the determination of subsurface properties, including pore pressure. Dvorkin et al. (1999) demonstrated that the V_P/V_S ratio (or Poisson's ratio) is strongly dependent on pore pressure. However, this theory can only be applied to a real case in the said location if V_S is accurately estimated around the seismogenic faults in the Nankai Trough off the Kii Peninsula. To accomplish this task, we estimate the V_P/V_S ratio in the sediment in the Nankai accretionary prism by using multicomponent ocean bottom seismometer (OBS) data acquired along the line extending from the trench to the seismogenic zone (Figures 1 and 2). This V_P/V_S profile across the accretionary prism further reveals the evolution of rock properties from the unconsolidated trough sediment to the consolidated rock around the seismogenic zone.

Usually, V_P/V_S ratio is estimate using the PS-converted reflected waves (e.g., MacBeth et al., 1992). Peacock et al. (2009) estimate V_S using PS-converted reflected waveforms of OBS data and downhole logging V_S data from the western Nankai Trough. However, it is difficult to identify the PS-converted reflection waveforms for each geological boundary in our study area because there is no dominant geological boundary within the sedimentary sequence and, further, because V_S was not measured in downhole logging. Therefore, we concentrated on the clearly observed PPS-refracted waves that are converted from the up-going P-waves to up-going S-waves at an interface below the receivers (Figure 3).

A recent drilling campaign of the Integrated Ocean Drilling Program (IODP) used borehole breakouts and core sample observations to show that the stress state (principal horizontal stress orientation) changes across the seismogenic megasplay fault (e.g., Lin et al., 2010). Maximum horizontal stress is parallel to the direction of plate subduction seaward of the megasplay fault and perpendicular to the direction of subduction landward of the megasplay fault. This stress orientation is related to the dynamic activities of the seismogenic fault. Therefore, revealing the stress orientation and its magnitude should provide useful information for monitoring seismogenic faults (e.g., Crampin et al., 2008). Several previous OBS studies proved to be instrumental (Haacke and Westbrook, 2006; Haacke et al., 2009; Peacock et al., 2009) because they report S-wave splitting occurring even in unconsolidated seafloor sediment. We also reveal the variations of the stress state across the Nankai accretionary prism by using S-wave splitting derived from the PPS-refracted wave.

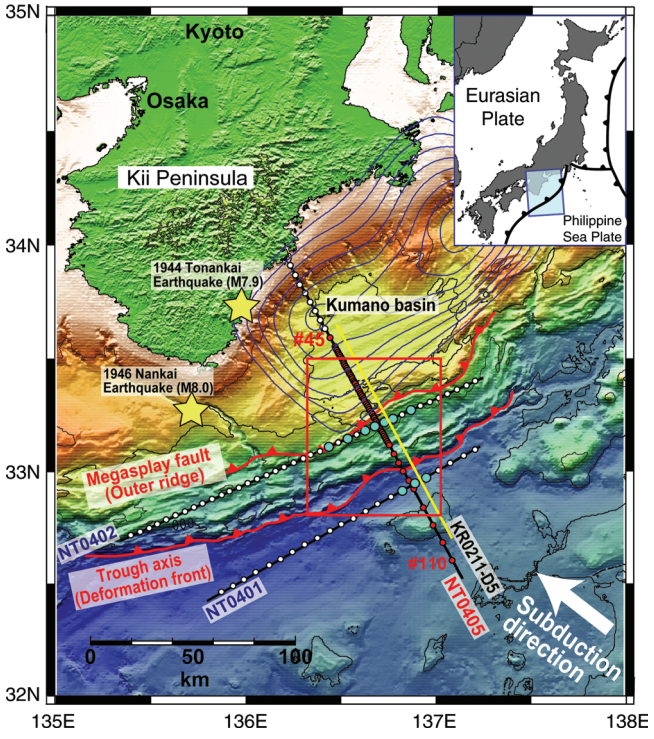

Figure 1. Bathymetric map of the Nankai Trough off the Kii Peninsula, southwest Japan. Black lines show locations of wide-angle OBS survey lines. Red (NT0405) and blue (NT0401 and NT0402) dots show the OBSs analyzed in this study. Yellow line indicates the location of the reflection profile (KR0211-D5) shown in Figure 2. Red lines represent the trough axis (deformation front) and seafloor trace of the megasplay fault (outer ridge). Yellow stars mark the estimated hypocenters of the 1944 Tonankai earthquake (M7.9) and the 1946 Nankai earthquake (M8.0). The red rectangle indicates the area shown in Figure 10. Blue contours around the Kumano basin show the coseismic slip distribution of the 1944 Tonankai earthquake (Kikuchi et al., 2003).

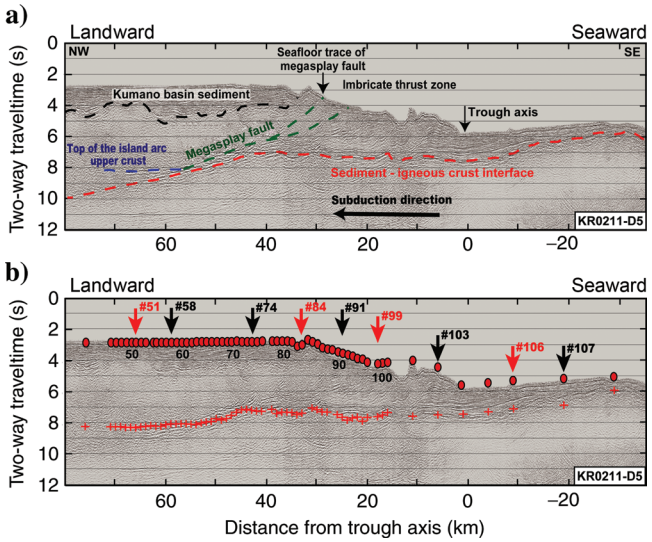

Figure 2. Seismic reflection profile (KR0211-D5) acquired parallel to OBS survey line NT0405. (a) Predominant geological boundaries on the seismic profile. The reflector marked "Top of the island arc upper crust" represents the boundary between the Neogene–Quaternary accretionary prism and the Cretaceous–Tertiary accretionary prism (Nakanishi et al., 2002). (b) The position of OBSs (red dots) and reflection points from the PS-converted surface (red crosses) on the seismic profile. The PS-converting surface corresponds to the oceanic crust surface (red dashed line in panel [a]), except in the landward region, where it represents the top of the island arc upper crust (blue dashed line in panel [a]). Red arrows indicate the OBS positions whose receiver gathers are shown in Figure 4. Black arrows indicate the OBS positions whose particle motions are shown in Figure 8.

GEOLOGIC SETTING

At the Nankai Trough, the Philippine Sea plate is subducting beneath Japanese Island at a convergence rate of 4–6.5 cm/year along 310–315° azimuth, as shown in Figure 1 (Seno et al., 1993; Miyazaki and Heki, 2001). Around the trough axis off Kii peninsula, an approximately 1.3-km-thick wedge of sand-rich trench sediments overlies about 1.1 km of Shikoku Basin sediments, which, in turn, overlie the igneous basement (Moore et al., 2009; and Figure 2a). The sediments above the plate boundary fault (décollement) are being accreted landward of the trough axis. Sequential imbricate thrusts are developed between the trough axis and a seismogenic megasplay fault (Figure 2a).

Seismic data (Figure 2) show a strong negative-polarity reflection representing the megasplay fault (e.g., Park et al., 2002; Moore et al., 2009). This feature at the megasplay fault has been interpreted to indicate elevated pore pressure in the fault zone (Park et al., 2002; Tsuru et al., 2005; Tsuji et al., 2006; Bangs et al., 2009). Seismic and tsunami inversions (Tanioka and Satake, 2001; Kikuchi et al., 2003) suggest that a rupture on this megasplay fault might have been generated in the 1944 Tonankai earthquake (M7.9) and the associated tsunami.

Landward of the megasplay fault, about 1 km of the Kumano Basin sequence (soft sediment) overlies the accretionary prism. The black dashed line in Figure 2a indicates the boundary between the Kumano basin sequence and the accretionary prism. In the Kumano Basin sequence immediately landward of the seafloor trace of the megasplay fault, there are normal faults striking nearly parallel to the strike of the megasplay fault (Park et al., 2002). In the deeper part of this landward region, a wedge-shaped unit appears to abut the subducting oceanic crust (blue dashed line in Figure 2a). This reflection is considered to represent the top of the island arc upper crust (Nakanishi et al., 2002; Tsuru et al., 2005).

MULTICOMPONENT OBS DATA

Data acquisition

In 2004, the Japan Agency for Marine-Earth Science and Technology acquired wide-angle OBS data with a high-density OBS array along a 175-km survey line traversing the Nankai Trough and crossing the coseismic rupture zone of the 1944 Tonankai earthquake (line NT0405 in Figure 1). The survey line was nearly parallel to the direction of the subduction of the Philippine Sea plate and perpendicular to the trough axis. A total of 74 OBSs were deployed along the survey line, at 1-km intervals in the center of the survey line and at 5-km intervals elsewhere, except for five OBSs at the seaward end of the line that were deployed at 10-km intervals. Each OBS had a three-component gimbal-mounted geophone system (4.5 Hz) and a hydrophone (Shinohara et al., 1993). A large airgun array (total volume approximately 200 l, pressure 14 MPa) was fired at 200-m intervals from R/V *Kaiyo*. Nakanishi et al. (2008) estimated the P-wave velocity distribution by using the vertical components of the OBS data.

Here we also used data from other OBS surveys (lines NT0401 and NT0402 in Figure 1) acquired parallel to the trough axis and perpendicular to line NT0405 (subduction direction). These OBS data were acquired with the same acquisition parameters as line NT0405 in 2004 (Kodaira et al., 2006). These trough-parallel seismic lines (NT0401 and NT0402) proved to be instrumental for estimating the influence of the shot-receiver direction (radial direction) on the estimated S-wave related properties (V_P/V_S ratio and S-wave splitting).

Data preparation

First, we determined the orientation of the OBS instrument axes by examining the horizontal components of particle motion of the direct water wave (the first-arrival wave at short offset). The strongest amplitude of the direct water wave is parallel to the survey line (the radial direction), which helped us calculate the radial and transverse components (Figure 4) for each OBS by applying waveform rotation. Because the transverse amplitude of the direct water wave was almost zero for the horizontal components, we could accurately determine the radial direction (accuracy ±3°).

The incident angle was almost vertical due to the slow P-wave velocity in the shallow sedimentary section. Because the P-refracted wave is not present in the horizontal components, the receiver tilt can be ignored in our analysis. We applied a band-pass filter, median filter, and predictive deconvolution to the OBS data before identifying each phase on the receiver gathers.

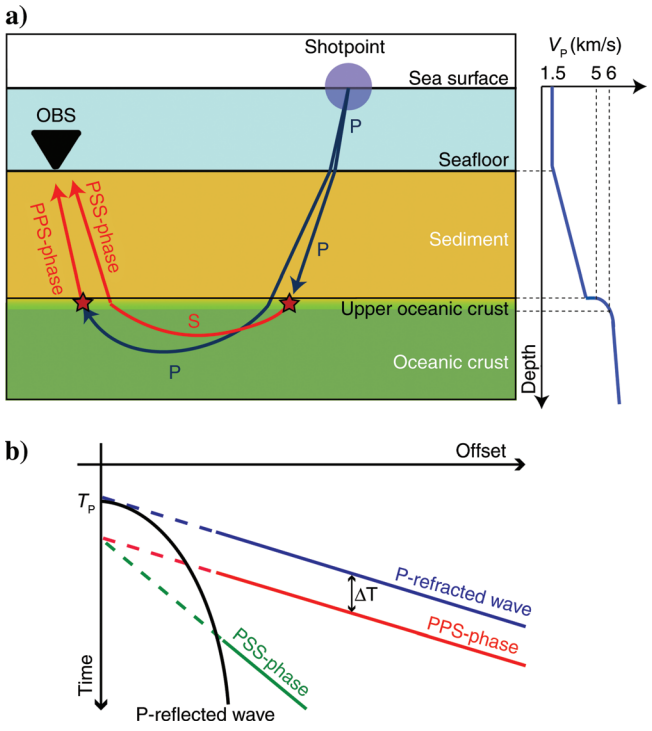

Figure 3. (a) Schematic raypath diagram showing the PPS- and PSS-phases. The PPS-phase is an S-wave converted at the upper oceanic crust beneath the OBS from an up-going refracted P-wave. The PSS-phase is an S-wave converted at the upper oceanic crust beneath the shotpoint from a down-going P-wave. Red stars indicate P- to S-wave conversion points. The PPS- and PSS-phases travel within basaltic crust with V_P (approximately 6.2 km/s) and V_S (approximately 3.4 km/s), respectively. Right-hand profile indicates the simplified P-wave velocity structures. (b) Schematic receiver gather showing P-refracted wave (blue), PPS-phase (red), PSS-phase (green), and P-reflected wave (black).

P-reflected and P-refracted waves

We clearly identified the P-refracted wave from the oceanic (basaltic) crust surface on the OBS receiver gathers (Figure 4) by comparing it to a time-domain reflection seismic profile acquired parallel to the OBS survey line (KR0211-D5; Figures 1 and 2). Because the raypaths can be considered almost vertical within the sedimentary section, the intercept time of the P-refracted wave is close to the zero-offset traveltime of the P-reflected wave on the reflection profile. The intercept times of the clearly observed P-refracted waveforms on the receiver gather were similar to the traveltimes of the P-reflection waveforms from the oceanic crust surface (Figure 4), which confirmed that we did analyze the P- and S-waves refracted around the crust surface (Figure 2b).

For the landward part of the survey line, the clear refracted waveforms are refracted at the top of the island arc upper crust (blue dashed line in Figure 2a; Nakanishi et al., 2002) or within the accreted sedimentary section (Figure 4d). Although it is difficult to identify the reflection waveforms in the landward part, the intercept time of the refracted wave is definitely located above the top of the island arc upper crust.

The apparent velocity of the P-refracted wave at the crust surface (approximately 6.2 km/s) is higher than the expected velocity of the uppermost oceanic crust (approximately 5 km/s; White et al., 1992). To reveal the reason for the high apparent velocity, we simulated elastic wave propagations using the finite-difference time-domain method for several realistic velocity models of upper oceanic crust with the 2-m grid interval (Figure 5). The results demonstrate that the faster apparent velocity may result from a rapid velocity increasing around the refracted surface (White et al., 1992). Velocities significantly increase at the uppermost oceanic crust, as well as at the sediment-crust interface (Figure 3a). Therefore, because the refracted surface does not have one sharp velocity contrast, the apparent velocity is influenced by the deeper lithology. The clearly observed refracted wave at the 20–40-km offset that we used in this study (Figure 4) is arguably refracted at the upper oceanic crust.

PPS- and PSS-phases

The PPS-phase results from the up-going refracted P-wave converted to the S-wave at the upper oceanic crust beneath the

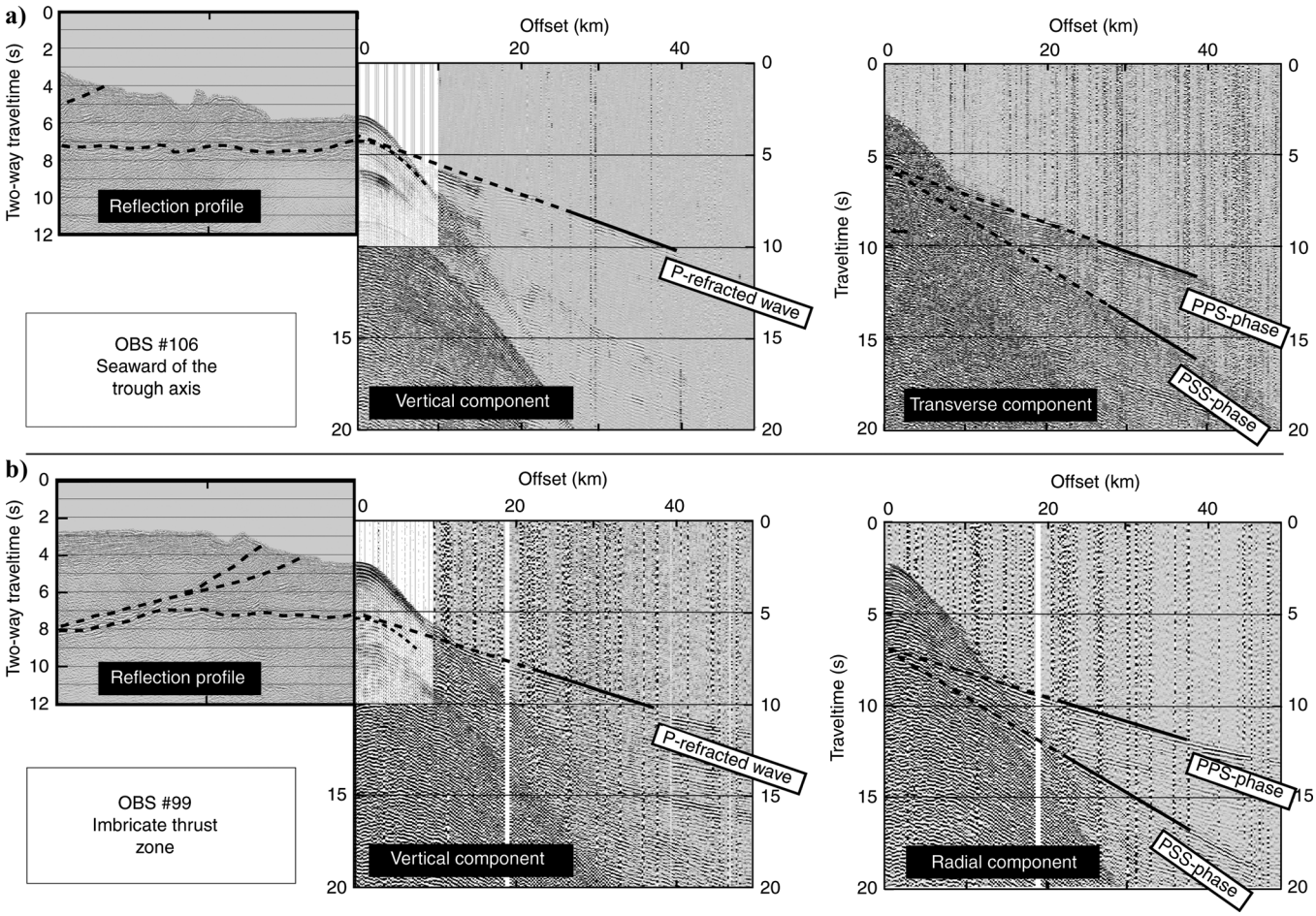

Figure 4. Comparison of OBS receiver gathers and stacked reflection profiles. Here we show receiver gathers of (a) seaward of the trough axis (OBS #106), (b) imbricate thrust zone (OBS #99).

receiver (Figure 3). It is clearly identified in the horizontal components of the receiver gathers (Figure 4). The PPS-phase is parallel to the P-refracted wave on receiver gathers, because both P-refracted and PPS-converted waves travel long distances through the oceanic crust as a P-wave.

We also recorded the PSS-phase (Figure 3), which is the result of the conversion of the down-going P-wave to the S-wave at the upper oceanic crust beneath the shotpoint. Because the PSS-phase travels a long distance as an S-wave, the PSS-phase shows a slower velocity on the receiver gather (Figure 4). From the estimated apparent velocity of PSS-phase (approximately 3.4 km/s), we confirmed that the PSS-phase travels within the oceanic crust as an S-wave and refracts at the uppermost oceanic crust below the receiver. Because the PSS-phase has a raypath similar to that of the PPS-phase, the former has a similar intercept time (Figures 3 and 4).

METHODS AND RESULTS

V_P/V_S ratio

If we assume that the P-refracted and PPS-converted waves have the same raypath, we can estimate the average V_P/V_S ratio within the sedimentary section beneath the OBS positions (Figures 6c) from (1) the zero-offset traveltime of the seafloor-reflected wave T_{Psf}, (2) the zero-offset traveltime of the reflected wave of the converted horizon T_P, and (3) the time lag ΔT between the P-refracted and PPS-converted waves:

$$\frac{V_P}{V_S} = \frac{2\Delta T + (T_P - T_{Psf})}{T_P - T_{Psf}}. \quad (1)$$

To determine T_P for each OBS, we compared the reflection waveforms on the OBS receiver gathers with the reflection from the sediment–crust interface on the poststacked reflection profile acquired parallel to the OBS survey line (red crosses in Figure 2b; Figure 4). To determine the time lag ΔT between the

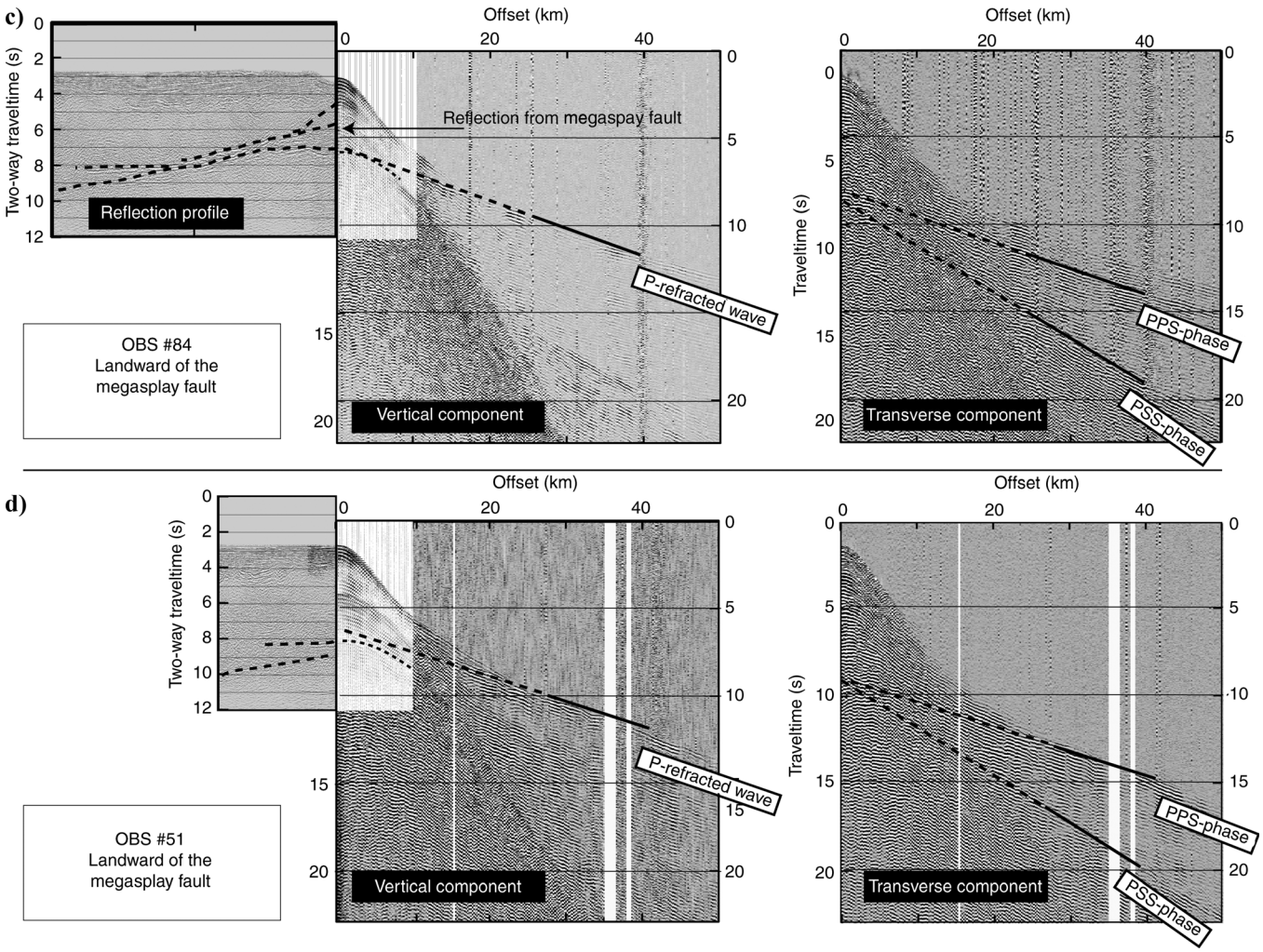

Figure 4. (cont.). (c) Landward of the splay fault (OBS #84), and (d) landward end of the profile (OBS #51). The intercept time of P-refracted wave is almost similar to the zero-offset of P-reflected wave because of steep incident angle. We analyzed the waveform using solid line parts. Because the PPS-phase is parallel to the P-refracted wave, we can use crosscorrelation for several traces to estimate the time lag between P-refracted and PPS-phase waveforms.

P-refracted and PPS-converted wave in equation 1, we first determined the P-wave refracted at the uppermost oceanic crust by considering the zero-offset traveltime of the reflected wave T_P, because the intercept time is closely located to T_P (Figures 3b and 4). Then, we applied crosscorrelation between P-refracted and the PPS-converted waves. Because they are parallel on the receiver gather, we can calculate time lag by cross-correlation of multitraces (approximately 100 traces; Figure 4) and enhance the signal. In the phase determination, we paid special attention to distinguish the PPS-phase with seafloor multiple (Takahashi et al., 2002).

As previously described, the clearly observed P-refracted wave is refracted at the contrast created by the rapid velocity increasing zone at the upper oceanic crust (not at the sediment-basement interface; Figure 5). To estimate a possible error in V_P/V_S originating from the uncertainty in the refracted surface (sediment-crust interface versus bottom of upper oceanic crust), let us assume that the sedimentary section is 5 km thick, with $V_P = 2.5$ km/s and $V_S = 1.19$ km/s ($V_P/V_S = 2.1$), and the upper oceanic crust is 1.5 km thick, with $V_P = 5.5$ km/s and $V_S = 3.05$ km/s ($V_P/V_S = 1.8$; Hyndman, 1979). The resulting maximum error is only 1.7% and, hence, can be neglected. We also confirmed the accuracy of our V_P/V_S values through an elastic simulation of wave propagation within a realistic velocity structure (Figure 5).

There is a possibility that the PPS-phase was converted to the S-waves within the sedimentary sequence above the upper oceanic crust, whereas in our ΔT calculations we assumed that the PPS-phase was converted at same horizon as the P-refracted surface (i.e., at the upper oceanic crust). Landward of the megasplay fault, there are several geological boundaries within the sedimentary sequence. When we assumed that the PPS-phase converted at the shallower sedimentary sequence and, hence, used smaller ΔT for V_P/V_S calculation, the estimated V_P/V_S ratio is lower than the average V_P/V_S ratio within the sedimentary sequence. However, there are no strong impedance contrasts in that part of the sedimentary sequence that would produce the clearly observed PPS-converted wave. Furthermore, we usually recognize one predominant waveform on the receiver gathers and this waveform usually corresponds to the first arrival on the horizontal components of many OBSs (Figure 4). Therefore, our first assumption that the predominant PPS-phase observed at the 20–40-km offset on the receiver gather was converted and refracted at the uppermost oceanic crust appears to be valid.

In contrast, around the megasplay fault, the PPS-phase converted at the uppermost oceanic crust is not the first arrival on the horizontal components (Figure 4c); the first-arrival waveforms have weak amplitude and seem to be converted within the sedimentary sequence (e.g., at the megasplay fault). Where it was difficult to identify the predominant PPS-phase on the receiver gather, we used the intercept time of PSS-converted wave for this purpose. Because the PSS-phase should be refracted at the same horizon as the P-refracted and PPS-converted wave beneath the receivers, the intercept times of PPS- and PSS-converted wave should be similar (Figure 3b). Therefore, it appears that the intercept time of the PSS-phase helps identify the PPS-phase.

Another source of errors may come from our assumption that the P-refracted and PPS-converted waves have identical raypaths. Because the raypath of the PPS-converted wave within the sedimentary sequence beneath the receiver is steeper (shorter path within the sedimentary sequence) than that of the P-refracted wave, the estimated V_P/V_S ratio is higher than the true V_P/V_S. We estimated this error to be also small (<2.5%) by taking into account the angle of incidence and the assumed impedance contrast at the conversion surface.

In the stratified sedimentary sequence seaward of the trough axis, our estimated V_P/V_S ratio is high ($V_P/V_S > 3$; Poisson's ratio approximately 0.44). However, the V_P/V_S ratio changes abruptly at the trough axis: it is approximately 2 (Poisson's ratio approximately 0.33) landward of the trough axis, where imbricate thrusts are developed. Following this, the V_P/V_S ratio increases

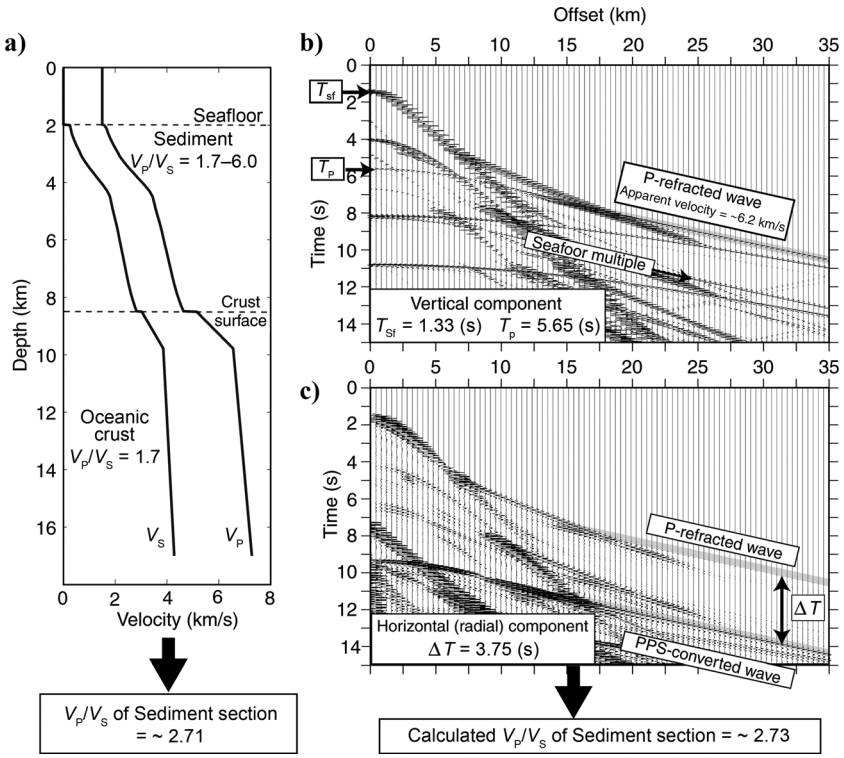

Figure 5. Elastic simulation for realistic velocity models using the finite-difference time-domain method. (a) Velocity model used for the elastic simulation. The P-wave velocity within sedimentary sequence is derived from a tomography-based approach (Nakanishi et al., 2008). Average V_P/V_S ratio within sedimentary section is approximately 2.71. Shown are the simulated receiver gathers of the (b) vertical component and (c) horizontal component. The average V_P/V_S ratio estimated by our proposed method (approximately 2.73) is consistent with true average V_P/V_S (approximately 2.71). The seafloor multiple exists parallel to the P-refracted and PPS-converted wave on the vertical component but not on the horizontal component.

gradually from the trough axis to the megasplay fault and afterward decreases with the increasing distance landward from the megasplay fault (Figure 6c). Therefore, there is a characteristic V_P/V_S ratio for each geological section (vertical black dashed lines in Figure 6). Furthermore, our estimated V_P/V_S values agree well with V_P/V_S derived from the intersecting OBS survey lines (lines NT0401 and NT0402; blue dots in Figure 6c). This consistency indicates that our estimated V_P/V_S ratio is robust and not affected by the survey line direction (i.e., dip of the converted surface).

Using the empirical relations of Castagna et al. (1985), we calculated the V_P/V_S ratio of mudrock (blue line in Figure 6c) from a P-wave interval (average) velocity within sedimentary sequence. The interval velocity was calculated from the P-wave velocity distribution derived by seismic tomography (Figure 6b; Nakanishi et al., 2008). Our estimated V_P/V_S ratio is slightly higher than that produced by the mudrock model seaward of the trough axis and lower than that in the imbricate thrust zone. Our estimated V_P/V_S ratio agrees well with the mudrock V_P/V_S ratio landward of the megasplay fault.

To compare our estimated V_P/V_S with existing laboratory-derived results, we constructed the relationship between V_P/V_S and V_P (Figure 7a) and that between V_P and V_S (Figure 7b). The V_P/V_S obtained in our analysis is a little higher than the laboratory-derived V_P/V_S (color squares in Figure 7). The difference might be explained by the presence of unconsolidated clay-rich sediments and by large-scale fractures or large-scale layered structures.

The relationship between V_P and V_S is nonlinear in the low-velocity range because unconsolidated (low-velocity) sequence has a small V_S (red line in Figure 7c; Vernik et al. 2002). Because our estimated V_P/V_S is averaged over large depth intervals, from shallow unconsolidated sequence to deep consolidated sequence, there is a possibility that the V_P/V_S ratio estimated in this study is affected by the high V_P/V_S at the shallower depths and has a high value. Therefore, we need to consider the scale of the measured interval when we compare the V_P/V_S ratio estimated from this method with laboratory-derived ratio.

S-wave splitting

When an S-wave propagates through an anisotropic elastic solid, it splits into two perpendicular polarizations, and these travel at different speeds (Crampin, 1981). It is generally agreed that seismic anisotropy within sediments is related to the amount of fracturing and the dominant orientation of those fractures (Kaneshima et al., 1988; Haacke and Westbrook, 2006; Haacke et al., 2009). For vertical cracks, the fast polarization direction coincides with the direction of crack alignment, whereas the time delay of the slower polarization provides information about crack density (Crampin, 1985). If cracks are produced by a regional tectonic stress field, the S-wave splitting can be used to estimate stress orientation and magnitude. In unconsolidated sequence, the observed stress-induced anisotropy (e.g., Mavko et al., 1995; Vega et al., 2006) may be due to the increasing contact of grain consolidation in the direction of the maximum stress (Johnson et al., 1998). However, seismic anisotropy can also be generated by the alignment of mineral grains (e.g., Nishizawa and Kanagawa, 2010) or bedding in sedimentary layers (e.g., Johnston and Christensen, 1995).

We first estimated the particle motion by comparing the radial and transverse components of the PPS-converted wave (Figure 8). Then, we calculated the fast S-wave polarization direction (Figure 9b) and traveltime difference of the PPS-converted waveforms. To obtain these two anisotropic parameters, we applied a crosscorrelation method; we constructed the crosscorrelation coherent on the relationship between rotation angle and time lag (e.g., Tadokoro et al., 1999). Because the traveltime difference was very small and because the signal-to-noise ratio was low, it was difficult to obtain stable results from a single pair of radial and transverse components. To improve the signal-to-noise ratio, we stacked the PPS-converted waveforms (approximately 100 traces) by considering apparent velocity and correcting arrival time on the receiver gather (Figure 4). This newly introduced stacking process enabled us to determine

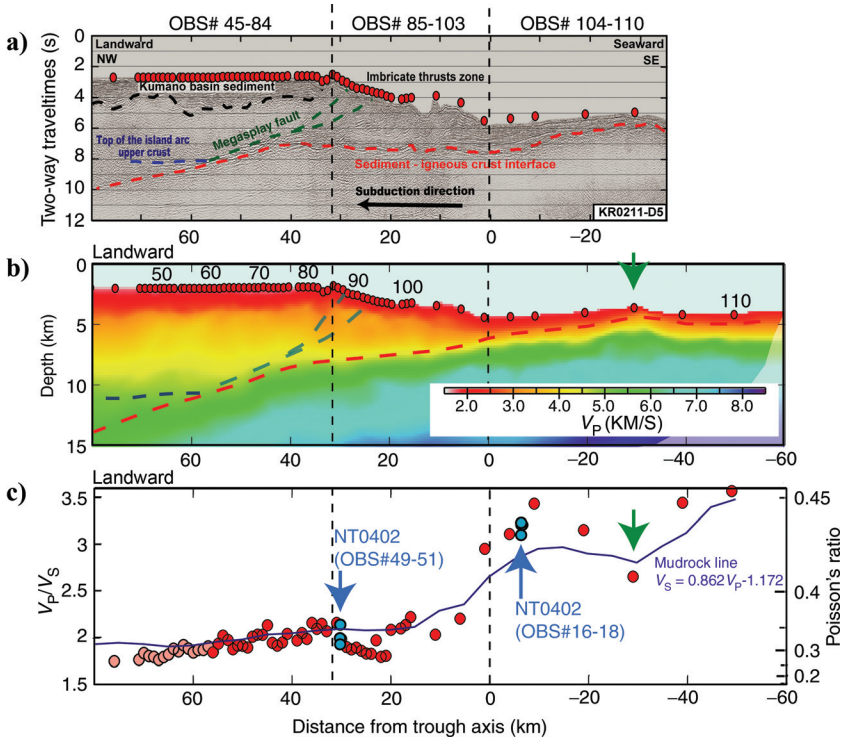

Figure 6. (a) Interpreted seismic reflection profile KR0211-D5 recorded parallel to OBS line NT0405. Red and blue dashed lines indicate the PS-converted surface (Figure 2b). Red dots at the seafloor reflection indicate OBS positions. (b) P-wave velocity within the Nankai accretionary prism estimated from the vertical component of OBS data (Nakanishi et al., 2008). OBS numbers are shown above the velocity profile. (c) V_P/V_S ratio along the OBS profile derived from traveltime differences between the P-refracted and PPS-converted waves. The pink dots on the landward end of the profile indicate a V_P/V_S ratio whose PS-converted surface is located around the top of the island arc upper crust (not at the upper basement). Blue dots indicate a V_P/V_S ratio derived from trough-parallel survey lines (NT0401 and NT0402).

the fast polarization direction and traveltime difference of the PPS- converted waveform. Although fast polarization direction and traveltime difference can be determined automatically through the above-mentioned process, the crosscorrelation is not sensitive to the polarization direction. Therefore, we checked their reliability by visually comparing waveforms (arrows in Figure 8).

We calculated the S-wave velocity anisotropy (Figure 9c) from (1) the traveltime difference between fast- and slow-polarization directions estimated via crosscorrelation and (2) up-going S-wave traveltime within sedimentary section (Equation 2):

$$\text{Velocity anisotropy} = (V_{Sf} - V_{Ss})/V_{Sf}. \quad (2)$$

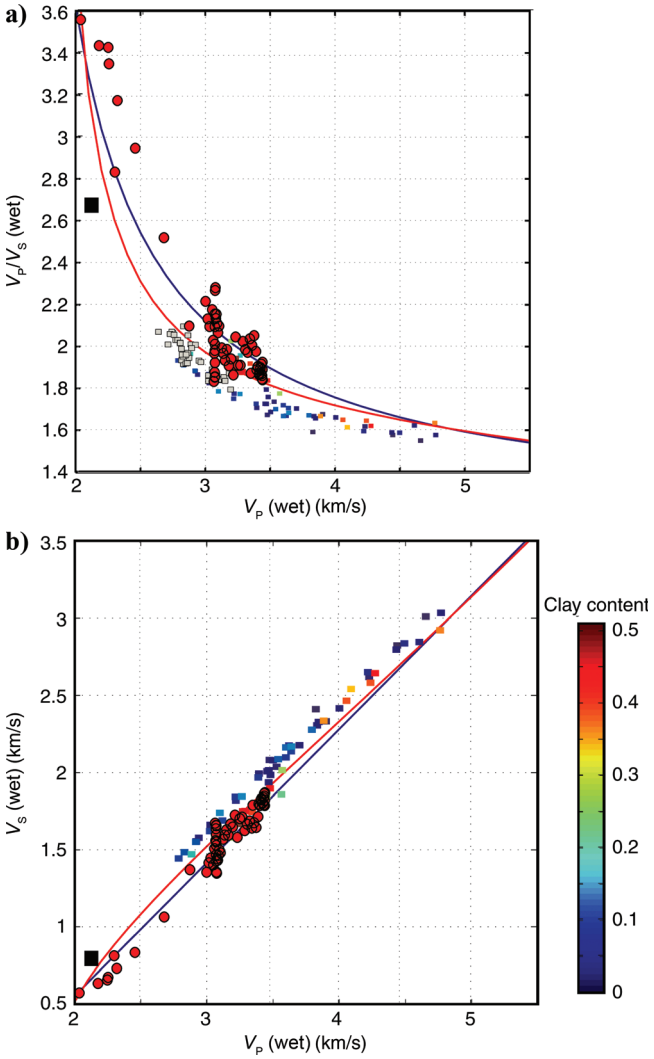

Figure 7. Relationships (a) between V_P/V_S and V_P and (b) between V_P and V_S. Red dots indicate points derived from OBS data analyzed in this study. Colored squares indicate laboratory data measured at 5 MPa (Han et al., 1986); the color scale indicates clay content. The black square indicates the relationship for soft Ottawa sand measured at 5 MPa. Troll samples (grey squares) were measured at 20 MPa (Yin, 1992). The blue line indicates the mudrock line of Castagna et al. (1985). The red line indicates Vernik's relation for soft marine sediment (Vernik et al., 2002).

where V_{Sf} is the S-wave velocity for fast polarization direction, and V_{Ss} is the S-wave velocity for slow polarization.

We observed large velocity anisotropy around the megasplay fault (Figure 9c). Although the fast polarization directions are somewhat scattered, the overall direction is normal to the subduction direction (transverse direction) landward of the megasplay fault (Figure 9b). Borehole breakout data from six boreholes along the OBS survey line (Lin et al., 2010) demonstrated that the horizontal principal stress directions are consistent with the fast polarization directions from OBS data (Figure 10); both directions change across the seafloor trace of the megasplay fault. Therefore, the fast polarization direction appears to reflect the stress state within the accretionary prism. Furthermore, we calculated these anisotropic parameters for the OBS data acquired along the direction normal to the subduction (NT0402; Figure 10). The results demonstrate that the fast polarization direction is the subduction direction seaward of the trace of the megasplay fault and subduction-normal direction landward of the megasplay fault. Therefore, because we obtained similar anisotropic trends from two intersecting OBS survey data (NT0402 and NT0405), the shooting direction apparently has little influence on the resulting anisotropy estimate.

To reveal the S-wave velocity anisotropy for the subduction direction, we estimated the traveltime difference between the radial (subduction direction) and transverse (subduction-normal direction) components and then calculated the velocity difference between the radial and transverse components (Figure 9d) via the following equation:

$$\text{Velocity difference} = (V_{SH} - V_{SV})/V_{SH}. \quad (3)$$

The velocity of the radial component (V_{SV}) is faster seaward of the megasplay fault; however, the velocity of the transverse component (V_{SH}) becomes fast immediately landward of the megasplay fault. This trend (Figure 9d) is consistent with our fast polarization direction and also with the velocity anisotropy (Figures 9b and c).

We should note that our results represent the cumulative effect of the anisotropic properties of all layers through which the up-going seismic waves have traveled (within the sedimentary sequence beneath each OBS station). Here, we assumed that the radial and transverse components originated at the same converting horizon (i.e., the sediment–igneous crust interface). However, because it is possible that the transverse component originated at a different position than the radial component, it may be difficult to precisely quantify this attribute.

GEOLOGICAL INTERPRETATION

Seaward of the trough axis (OBS #104–110)

The V_P/V_S ratio seaward of the trough axis is >3 and is higher than the V_P/V_S of soft Ottawa sand (black dots in 7; Yin, 1992). Zimmer et al. (2002) reported high V_P/V_S for the unconsolidated sediments at small effective stress conditions from laboratory experiments. Therefore, we conclude that the high V_P/V_S ratio primarily indicates unconsolidated (uncompacted) sequence. Because the V_P/V_S ratio is also controlled by clay content (Figure 7), the unconsolidated (hemipelagic) clay-rich sequence seaward of the

trough axis can explain the high V_P/V_S (Peacock et al., 2009). A low V_P/V_S ratio 27 km seaward from the trough axis (green arrows in Figure 6) may indicate relatively well-consolidated sediment above a basement high that could have been uplifted and exposed at the seafloor by dynamic displacement on reverse faults within oceanic crust (Tsuji et al., 2009).

Seaward of the trough axis, the estimated velocity anisotropy is very small, and the fast S-wave polarization directions are scattered. Therefore, the stratified sedimentary sequence seaward of the trough axis can be modeled by a transversely isotropic with vertical symmetry axis (VTI) medium (Figure 11). Velocity anisotropy 10 km seaward from the trough axis (OBS #106) is strong (black arrow in Figure 9), and the fast polarization direction is perpendicular to the radial direction. The seismic reflection profile and seafloor geometry indicate the existence of a fault induced by intraoceanic fault displacement (Tsuji et al., 2009) beneath the OBS (yellow line in Figure 10). This observation demonstrates that the fast S-wave polarization direction is sensitive to the fault plane orientation.

Imbricate thrust zone from trough axis to megasplay fault (OBS #85–103)

The abrupt change in the V_P/V_S ratio at the trough axis (Figure 6c) is probably caused by sediment consolidation associated with the accretion process (reverse faulting due to horizontal compaction) because the V_P/V_S ratio is usually considerably affected by porosity, as well as the effective stress. Therefore, compaction-driven dewatering would be concentrated near the trough axis (Spinelli and Saffer, 2007). Furthermore, because the sand-rich trench sediment (low V_P/V_S) is deposited by turbidity currents that flow from the coast to the trough axis and is accreted landward of the trough axis, the presence of relatively sand-rich accreted sediment landward of the trough axis may act to further reduce the V_P/V_S ratio.

The small increase in V_P/V_S just seaward of the megasplay fault (Figure 6c) may indicate abnormal pore pressure (decreasing effective stress) because the V_P/V_S ratio increases with increasing pore pressure in wet sediment (e.g., Dvorkin et al., 1999). In this region, anomalously low V_P below seaward extension of the megasplay fault was identified from seismic reflection data by Park et al. (2010). Furthermore, there is a possibility that intensive fractures associated with the megasplay fault act to increase the V_P/V_S ratio. From our S-wave splitting analysis, the velocity anisotropy appears to be especially strong as the location approaches the megasplay fault (Figure 9c). This indicates that, arguably, the fractures are well developed around this fault.

In the seaward part of the imbricate thrust zone, the fast S-wave polarization direction is along the subduction. Because the sediment in this region is not consolidated and because the principal stress direction is nearly parallel to the subduction (Figure 11), the seismic anisotropy seems to be influenced by the principal horizontal stress (Vega et al., 2006; Mavko et al., 1995) mainly by the stiffening of the grain contacts along the principal stress direction (Johnson et al., 1998). Because the imbricate thrust region is relatively sand-rich sequence, the stress-induced anisotropy seems to be significant as compared with the mud-rich sequence.

However, the fast S-wave polarization direction is progressing from the radial direction (along the subduction) to the transverse direction (subduction-normal) around the megasplay fault (Figure 9b). Furthermore, V_{SH} increases more than V_{SV} as the fault is approached (Figure 9d), which suggests that both the preferred orientation of faults and the principal stress

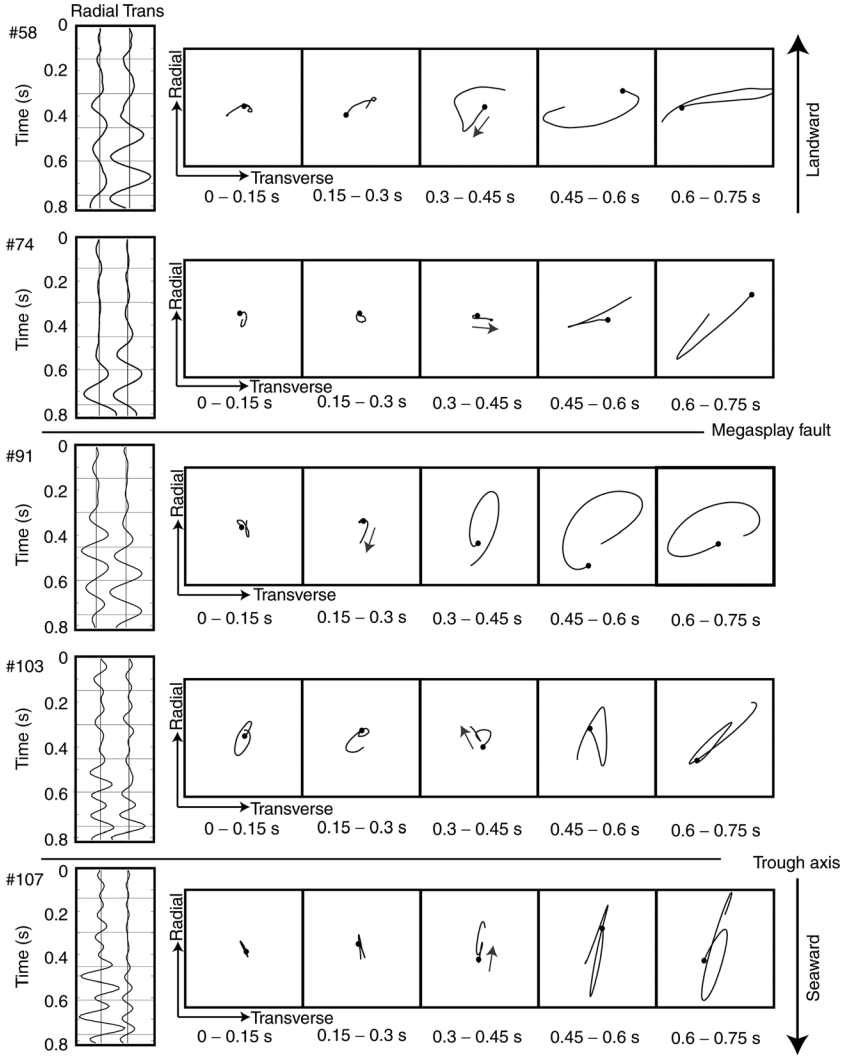

Figure 8. From left to right: Enlarged examples of PPS-converted waveforms (radial and transverse components) and particle motion for five 150-ms-long time windows. Horizontal and vertical axes in the particle motion diagrams represent transverse and radial components, respectively. The first sample in each time window is marked with a black dot. Arrows indicate fast S-wave polarization direction.

direction are oblique to the subduction direction near the megasplay fault.

Landward of the megasplay fault (OBS #45–84)

The steady landward decrease of V_P/V_S from the seafloor trace of the megasplay fault to the landward end of the survey line may reflect increasing sediment consolidation. Cementation associated with heating and increasing pressure would promote consolidation in the landward direction.

The relatively high V_P/V_S trend landward of the fault (higher than the imbricate thrust zone) may reflect unconsolidated sediment in the Kumano Basin overlying the accretionary prism, the strong deformation (fracturing) of the accretionary prism, or both. Well data from the IODP (Expedition 314 Scientists, 2009) revealed that the accretionary prism beneath the Kumano Basin is greatly deformed. Although there is a possibility that overpressure beneath the megasplay fault (Tsuru et al., 2005; Tsuji et al., 2006) acts to increase the V_P/V_S ratio, the overpressure (high V_P/V_S) zone beneath the fault is thin in this landward region (Figure 2). Therefore, the contribution of the overpressure to the high V_P/V_S should not be significant in this region. Furthermore, it is difficult to accurately identify the location of PS-converted surface in this region (above or beneath the megasplay faults).

The fast S-wave polarization direction is almost perpendicular to the subduction immediately landward of the megasplay fault (Figure 9b). This observation demonstrates that the direction of the principal horizontal stress changes across the megasplay fault. The development of trough-parallel normal faults in the Kumano Basin (landward of the megasplay fault) also reflects this change. We can, therefore, treat this region as an HTI (transversely isotropic with horizontal symmetry axis) medium whose axis of symmetry is horizontal and parallel to the subduction (Figure 11).

The above anisotropic characteristics are not clearly evident at the landward end of the OBS survey line (Figure 9); the degree of velocity anisotropy appears to decrease landward. This indicates that the major changes of stress orientation occur only in the proximity to the megasplay fault.

CONCLUSIONS

We summarize here the main results obtained in this study:

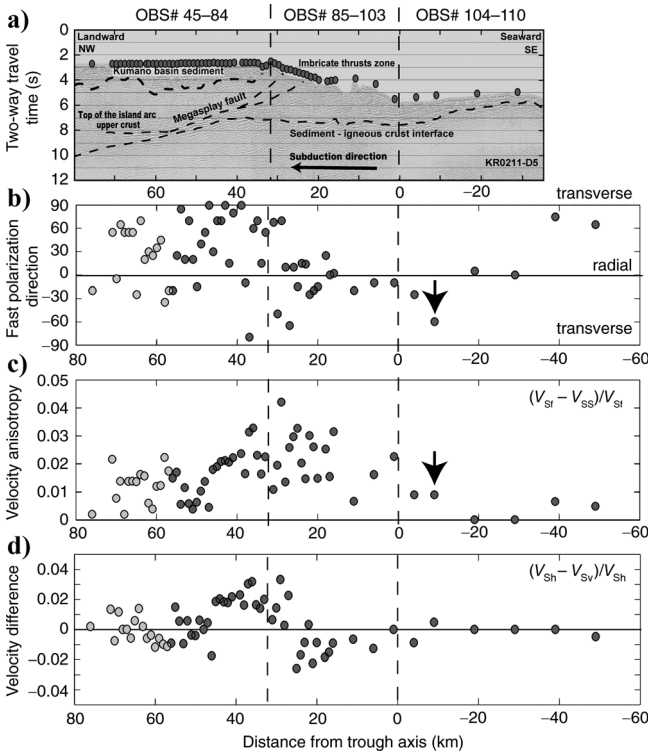

Figure 9. Anisotropic parameters along the OBS survey line (NT0405). (a) Interpreted seismic reflection profile KR0211-D5 recorded parallel to OBS line NT0405. (b) Fast S-wave polarization direction. Light gray dots on the landward end of the profile indicate anisotropic properties whose PS-converted surface is located around the top of the island arc upper crust. (c) S-wave velocity anisotropy. (d) Velocity difference between radial component (subduction direction) and transverse component (subduction-normal direction).

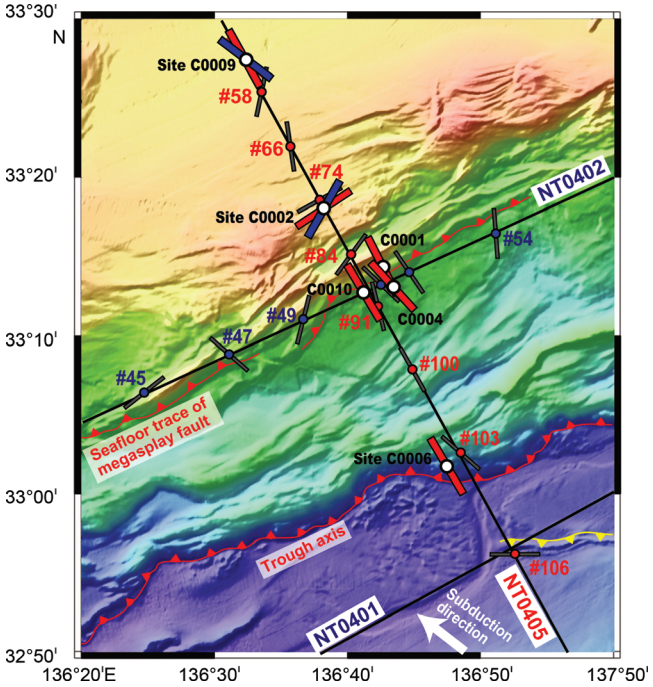

Figure 10. Comparison of horizontal principal stress direction (SH1) derived from borehole breakouts (red and blue bars; Lin et al., 2010) and fast polarization direction (gray bars) from OBS data (NT0405 and NT0402 data). The red bars show stress orientations in the accretionary prism, and the blue bars show stress orientations in the shallow Kumano basin. The bathymetric map corresponds to the red rectangle in Figure 1. The fast polarization directions change across the megasplay fault and are almost consistent with the principal stress direction. The yellow line shows fault induced by intraoceanic fault displacement (Tsuji et al., 2009). Fast S-wave polarization direction at OBS #106 agrees with the fault strike.

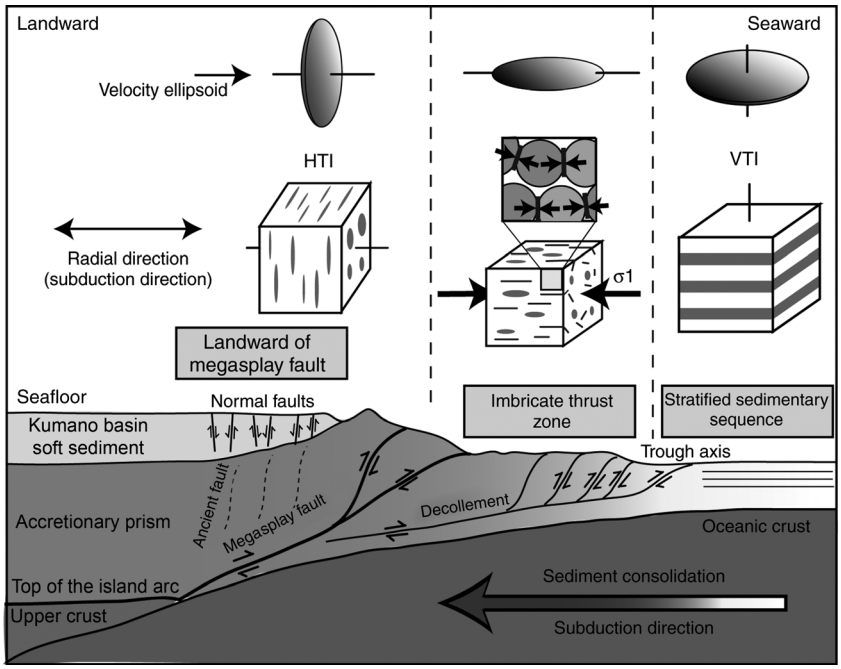

Figure 11. Geological interpretation of the estimated V_P/V_S and seismic anisotropy along OBS survey line NT0405. From the estimated V_P/V_S ratio and anisotropic parameters, we divide three geological sections: (1) stratified sedimentary sequence seaward of the trough axis, (2) imbricate thrust zone between trough axis and megasplay fault, and (3) landward of the megasplay fault.

1) We measured the V_P/V_S ratio and S-wave splitting across the Nankai Trough and accretionary prism from clearly observed PPS-refracted waves recorded by an OBS system. The method we used may be instrumental for determining the average V_P/V_S ratio above a dominant PS-converting subsurface interface.
2) We showed that the V_P/V_S ratio landward of the trough axis (approximately 2) is smaller than that seaward of the trough axis (>3). This abrupt change of V_P/V_S at the trough axis is attributed to sediment compaction associated with the accretion process.
3) V_P/V_S ratio seems to increase seaward of the megasplay fault due to the abnormal pore pressures in the footwall of the fault.
4) The V_P/V_S values obtained here are slightly higher than the laboratory-derived V_P/V_S data for comparable sediments. These high V_P/V_S estimates might reflect a mud-dominated sedimentary sequence, large-scale structures, or both.
5) By stacking the converted waveforms and improving the signal-to-noise ratio, we extracted the S-wave fast polarization direction and the velocity anisotropy.
6) We found that the fast S-wave polarization direction is the transverse direction (subduction-normal direction) near the megasplay fault and that velocity anisotropy is largest in this region. These observations suggest that the preferred fracture orientation, as well as the principal stress orientation, is oblique to the subduction near the megasplay fault.

ACKNOWLEDGMENTS

We used OBS data (Lines NT0401, NT0402 and NT0405) and multichannel seismic reflection data (KR0211-D5) acquired by the Japan Agency for Marine-Earth Science and Technology (JAMSTEC). G. Fujie (JAMSTEC), R. Hino (Tohoku University), and anonymous reviewers gave us helpful comments for the OBS analysis and interpretations. This research was supported by the Grant-in-Aid for Young Scientists (B) program from the Japan Society for the Promotion of Science (JSPS) (20760568), the JSPS Excellent Young Researcher Overseas Visit Program (21-5338), and a Grant-in-Aid for Scientific Research on Innovative Areas (21107003).

REFERENCES

Ando, M., 1975, Source mechanisms and tectonic significance of historical earthquake along the Nankai Trough, Japan: Techtonophysics, **27**, 119–140, doi:10.1016/0040–1951(75)90102-X.

Bangs, N. L., G. F. Moore, S. P. S. Gulick, E. M. Pangborn, H. J. Tobin, S. Kuramoto, and A. Taira, 2009, Broad, weak regions of the Nankai Megathrust and implications for shallow coseismic slip: Earth and Planetary Science Letters, **284**, no. 1–2, 44–49, doi:10.1016/j.epsl.2009.04.026.

Bangs, N. L., T. H. Shipley, S. P. S. Gulick, G. F. Moore, S. Kuromoto, and Y. Nakamura, 2004, Evolution of the Nankai Trough décollement from the Trench into the seismogenic zone: Inferences from three-dimensional seismic reflection imaging: Geology, **32**, 273–276, doi:10.1130/G20211.2.

Castagna, J. P., M. L. Batzle, and R. L. Eastwood, 1985, Relationships between compressional-wave and S-wave velocities in clastic silicate rocks: Geophysics, **50**, 571–581, doi:10.1190/1.1441933.

Crampin, S., 1981, A review of wave motion in anisotropic and cracked elastic media: Wave Motion, **3**, no. 4, 343–391, doi:10.1016/0165–2125(81)90026–3.

———, 1985, Evaluation of anisotropy by shear-wave splitting: Geophysics, **50**, 142–152, doi:10.1190/1.1441824.

Crampin, S., Y. Gao, and S. Peacock, 2008, Stress-forecasting (not predicting) earthquakes: A paradigm shift?: Geology, **36**, no. 5, 427–430, doi:10.1130/G24643A.1.

Dvorkin, J., G. Mavko, and A. Nur, 1999, Overpressure detection from compressional- and shear-wave data: Geophysical Research Letters, **26**, 3417–3420, doi:10.1029/1999GL008382.

Expedition 314 Scientists, 2009, Expedition 314 Site C0002, *in* M. Kinoshita, H. Tobin, J. Ashi, G. Kimura, S. Lallement, E. J. Screaton, D. Curewitz, H. Masago, K. T. Moe, and the Expedition 314/315/316 Scientists, Proc. IODP 314/315/316, doi:10.2204/iodp.proc.314315316.114.2009.

Haacke, R. R., and G. K. Westbrook, 2006, A fast, robust method for detecting and characterizing azimuthal anisotropy with marine PS converted waves, and its application to the west Svalbard continental slope: Geophysical Journal International, **167**, 1402–1412, doi:10.1111/j.1365–246X.2006.03186.x.

Haacke, R. R., G. K. Westbrook, and S. Peacock, 2009, Layer stripping of shear-wave splitting in marine PS waves: Geophysical Journal International, **176**, 782–804, doi:10.1111/j.1365–246X.2008.04060.x.

Han, D., A. Nur, and D. Morgan, 1986, Effects of porosity and clay content on wave velocities in sandstone: Geophysics, **51**, 2093–2107, doi:10.1190/1.1442062.

Hyndman, R. D., 1979, Poisson's ratio in the oceanic crust — A review: Tectonophysics, **59**, no. 1–4, 321–333, doi:10.1016/0040-1951(79)90053-2.

Johnson, D. L., L. M. Schwartz, D. Elata, J. G. Berryman, B. Hornby, and A. N. Norris, 1998, Linear and nonlinear elasticity of granular media: Stress-induced anisotropy of a random sphere pack: Journal of Applied Mechanics, **65**, no. 2, 380–388, doi:10.1115/1.2789066.

Johnston, J. E., and N. I. Christensen, 1995, Seismic anisotropy of shales: Journal of Geophysical Research, **100**, B4, 5991–6003, doi:10.1029/95JB00031.

Kaneshima, S., M. Ando, and S. Kimura, 1988, Evidence from shear-wave splitting for the restriction of seismic anisotropy to the upper crust: Nature, **335**, no. 6191, 627–629, doi:10.1038/335627a0.

Kikuchi, M., M. Nakamura, and K. Yoshikawa, 2003, Source rupture processes of the 1944 Tonankai earthquake and the 1945 Mikawa

earthquake derived from low-gain seismograms: Earth, Planets, and Space, **55**, 159–172.
Kodaira, S., T. Hori, A. Ito, S. Miura, G. Fujie, J.-O. Park, T. Baba, H. Sakaguchi, and Y. Kaneda, 2006, A cause of rupture segmentation and synchronization in the Nankai trough revealed by seismic imaging and numerical simulation: Journal of Geophysical Research, **111**, B0901, doi:10.1029 /2005JB004030.
Lin, W., M.-L. Doan, J. C. Moore, L. McNeill, T. B. Byrne, T. Ito, D. Saffer, M. Conin, M. Kinoshita, Y. Sanada, K. T. Moe, E. Araki, H. Tobin, D. Boutt, Y. Kano, N. W. Hayman, P. Flemings, G. J. Huftile, D. Cukur, C. Buret, A. M. Schleicher, N. Efimenko, K. Kawabata, D. M. Buchs, S. Jiang, K. Kameo, K. Horiguchi, T. Wiersberg, A. Kopf, K. Kitada, N. Eguchi, S. Toczko, K. Takahashi, and Y. Kido, 2010, Present-day principal horizontal stress orientations in the Kumano forearc basin of the southwest Japan subduction zone determined from IODP NanTroSEIZE drilling Site C0009: Geophysical Research Letters, **37**, no. 13, L13303, doi:10.1029/2010GL043158.
MacBeth, C., X. Y. Li, S. Crampin, and M. C. Mueller, 1992, Detecting lateral variability in fracture parameters from surface data: 62nd Annual International Meeting, SEG, Expanded Abstracts, 816–819.
Mavko, G., T. Mukarji, and N. Godfrey, 1995, Predicting stress-induced velocity anisotropy in rocks: Geophysics, **60**, 1081–1087, doi:10.1190/1.1443836.
Miyazaki, S., and K. Heki, 2001, Crustal velocity field of southwest Japan: Subduction and arc–arc collision: Journal of Geophysical Research, **106**, B3, 4305–4326, doi:10.1029/2000JB900312.
Moore, G., J.-O. Park, N. L. Bang, S. P. Gulick, H. J. Tobin, Y. Nakamura, S. Sato, T. Tsuji, T. Yoro, H. Tanaka, S. Uraki, Y. Kido, Y. Sanada, S. Kuramoto, and A. Taira, 2009, Structural and seismic stratigraphic framework of the NanTroSEIZE Stage 1 transect: Kumano 3-D seismic survey, IODP Expedition Results, 314/315/316.
Moore, G. F., T. H. Shipley, P. L. Stoffa, D. E. Karig, A. Taira, S. Kuramoto, H. Tokuyama, and K. Suyehiro, 1990, Structure of the Nankai Trough accretionary zone from multichannel seismic reflection data: Journal of Geophysical Research, **95**, B6, 8753–8765, doi:10.1029/JB095iB06p08753.
Moore, J. C., and D. M. Saffer, 2001, Updip limit of the seismogenic zone beneath the accretionary prism of southwest Japan: An effect of diagenetic to low-grade metamorphic processes and increasing effective stress: Geology, **29**, 183–186, doi:10.1130/0091–7613(2001)029<0183:ULOTSZ>2.0.CO;2.
Nakanishi, A., S. Kodaira, S. Miura, A. Ito, T. Sato, J.-O. Park, Y. Kido, and Y. Kaneda, 2008, Detailed structural image around splay-fault branching in the Nankai subduction seismogenic zone: Results from a high-density ocean bottom seismic survey: Journal of Geophysical Research, **113**, B03105, doi:10.1029/2007JB004974.
Nakanishi, A., S. Kodaira, J.-O. Park, and Y. Kaneda, 2002, Deformable backstop as seaward end of coseismic slip in the Nankai Trough seismogenic zone: Earth and Planetary Science Letters, **203**, no. 1, 255–263, doi:10.1016/S0012–821X(02)00866-X.
Nishizawa, O., and K. Kanagawa, 2010, Seismic velocity anisotropy of phyllosilicate-rich rocks: Characteristics inferred from experimental and crack-model studies of biotite-rich schist: Geophysical Journal International, **182**, 375–388.
Park, J.-O., G. Fujie, L. Wijerathne, T. Hori, S. Kodaira, Y. Fukao, G. F. Moore, N. L. Bangs, S. Kuramoto, and A. Taira, 2010, A low-velocity zone with weak reflectivity along the Nankai subduction zone: Geology, **38**, 283–286, doi:10.1130/G30205.1.
Park, J.-O., T. Tsuru, S. Kodaira, P. R. Cummins, and Y. Kaneda, 2002, Splay fault branching along the Nankai subduction zone: Science, **297**, 1157–1160, doi:10.1126/science.1074111.
Peacock, S., G. K. Westbrook, and G. Bais, 2009, S-wave velocities and anisotropy in sediments entering the Nankai subduction zone, offshore Japan: Geophysical Journal International, **180**, 743–758, doi:10.1111/j.1365–246X.2009.04430.x.
Scholz, C. H., 1998, Earthquakes and friction lows: Nature, **391**, no. 6662, 37–42, doi:10.1038/34097.
Seno, T., S. Stein, and A. E. Gripp, 1993, A model for the motion of the Philippine Sea plate consistent with NUVEL–1 and geological data: Journal of Geophysical Research, **98**, B10, 17941–17948, doi:10.1029/93JB00782.
Shinohara, M., K. Suyehiro, S. Matsuda, and K. Ozawa, 1993, Digital recording ocean bottom seismometer using portable digital audio tape recorder: Journal of the Japan Society for Marine Surveys and Technology, **5**, 21–31.
Spinelli, G. A., and D. M. Saffer, 2007, Trench-parallel fluid flow in subduction zones resulting from temperature differences: Geochemistry Geophysics Geosystems, **8**, Q09009, doi:10.1029/2007GC001673.
Tadokoro, K., M. Ando, and Y. Umeda, 1999, S wave splitting in the aftershock region of the 1995 Hyogo-ken Nanbu earthquake: Journal of Geophysical Research, **104**, B1, 981–991, doi:10.1029/1998JB900024.
Takahashi, N., S. Kodaira, A. Nakanishi, J.-O. Park, S. Miura, T. Tsuru, Y.Kaneda, K. Suehiro, H. Kinoshita, N. Hirata, and T. Iwasaki, 2002, Seismic structure of western end of the Nankai trough seismogenic zone: Journal of Geophysical Research, **107**, B10, 2212–2230, doi:10.1029/2000JB000121.
Tanioka, Y., and K. Satake, 2001, Detailed coseismic slip distribution of the 1944 Tonankai earthquake estimated from tsunami waveforms: Geophysical Research Letters, **28**, 1075–1078, doi:10.1029/2000GL012284.
Tobin, H. J., and D. M. Saffer, 2009, Elevated fluid pressure and extreme mechanical weakness of a plate boundary thrust, Nankai Trough subduction zone: Geology, **37**, 679–682, doi:10.1130/G25752A.1.
Tsuji, T., G. Kimura, S. Okamoto, F. Kono, H. Mochinaga, T. Saeki, and H. Tokuyama, 2006, Modern and ancient seismogenic out-of-sequence thrusts in the Nankai accretionary prism: Comparison of laboratory-derived physical properties and seismic reflection data: Geophysical Research Letters, **33**, L18309, doi:10.1029/2006GL027025.
Tsuji, T., T. Matsuoka, Y. Yamada, Y. Nakamura, J. Ashi, H. Tokuyama, S. Kuramoto, and N. L. Bangs, 2005, Initiation of plate boundary slip in the Nankai Trough off the Muroto peninsula, southwest Japan: Geophysical Research Letters, **32**, L12306, doi:10.1029/2004GL021861.
Tsuru, T., S. Miura, J.-O. Park, A. Ito, G. Fujie, Y. Kaneda, T. No, T. Katayama, and J. Kasahara, 2005, Variation of physical properties beneath a fault observed by a two-ship seismic survey off southwest Japan: Journal of Geophysical Research, **110**, B5, B05405, doi:10.1029/2004JB003036.
Tsuji, T., J.-O. Park, G. Moore, S. Kodaira, Y.Fukao, S. Kuramoto, and N. Bangs, 2009, Intraoceanic thrusts in the Nankai Trough off the Kii Peninsula: Implications for intraplate earthquakes: Geophysical Research Letters, **36**, L06303, doi:10.1029/2008GL036974.
Tsuji, T., H. Tokuyama, P. Costa-Pisani, and G. Moore, 2008, Effective stress and pore pressure in the Nankai accretionary prism off the Muroto Peninsula, southwestern Japan: Journal of Geophysical Research, **113**, B11401, doi:10.1029/2007JB005002.
Vega, S., G. Mavko, A. Nur, and M. Prasad, 2006, Detection of stress-induced velocity anisotropy in unconsolidated sands: The Leading Edge, **25**, 252–256, doi:10.1190/1.2184090.
Vernik, L., D. Fisher, and S. Bahret, 2002, Estimation of net-to-gross from P and S impedance in deepwater turbidites: The Leading Edge, **21**, 380–387, doi:10.1190/1.1471602.
White, R. S., D. McKenzie, and R. K. O'Nions, 1992, Oceanic crustal thickness from seismic measurements and rare earth element inversions: Journal of Geophysical Research, **97**, B13, 19,683–19,715, doi:10.1029/92JB01749.
Yin, H., 1992, Acoustic velocity and attenuation of rocks: Isotropy, intrinsic anisotropy, and stress-induced anisotropy: Ph.D. thesis, Stanford University.
Zimmer, M., M. Prasad, and G. Mavko, 2002, Pressure and porosity influences on V_P-V_S ratio in unconsolidated sands: The Leading Edge, **21**, 178–183, doi:10.1190/1.1452609.